Imaging the Electron Wave Function in Self-Assembled Quantum Dots

E. E. Vdovin,[1]* A. Levin,[1] A. Patanè,[1] L. Eaves,[1]† P. C. Main,[1] Yu. N. Khanin,[2] Yu. V. Dubrovskii,[1]* M. Henini,[1] G. Hill[3]

Magnetotunneling spectroscopy is used as a noninvasive and nondestructive probe to produce two-dimensional spatial images of the probability density of an electron confined in a self-assembled semiconductor quantum dot. The technique exploits the effect of the classical Lorentz force on the motion of a tunneling electron and can be regarded as the momentum (*k*) space analog of scanning tunneling microscopy imaging. The images reveal the elliptical symmetry of the ground state and the characteristic lobes of the higher energy states.

A quantum dot (QD) is a nanostructure that can confine the motion of an electron in all three spatial dimensions. This gives rise to a set of discrete and narrow electronic energy levels, similar to those in atomic physics. The sharp line optical absorption and emission spectra of semiconductor QDs produced by Stranski-Krastanow self-assembly (*1*–*4*) or by colloidal synthesis (*5*, *6*) have now been extensively studied, but to date, there have been no reported measurements of the detailed spatial form of the wave functions of the ground and excited state levels of QDs. Although scanning tunneling microscopy (STM) and related techniques (*7*–*9*) are powerful tools for imaging electronic states on or close to condensed matter surfaces, a different technique is required for QDs, which are embedded deep below the surface. We describe how magnetotunneling spectroscopy can be used as a noninvasive and nondestructive probe to produce full spatial maps of the wave function of the ground and excited states of electrons in a QD. The technique therefore serves as a test bed for theoretical models of the electronic states in this type of nanostructure. In particular, model calculations (*10*) of probability density distributions for the ground and excited states of a QD (Fig. 1A) can be compared with our measurements.

In our device, a layer of InAs self-assembled QDs is embedded in the center of an undoped 12-nm GaAs quantum well (QW), which is sandwiched between two 8.3-nm $Al_{0.4}Ga_{0.6}As$ tunnel barriers. The layer of InAs QDs was grown by depositing 2.3 monolayers of InAs. Undoped GaAs spacer layers of 50-nm width separate the barriers from two contact layers with graded *n*-type doping (*11*). The device acts as a resonant tunneling diode in which electrons can tunnel into the QD from a doped contact layer on the opposite side of the barrier. Here we focus on a structure grown on a (311)B-oriented GaAs substrate, although we obtained similar results for dots grown on (100)-oriented GaAs. For comparison, we also studied two control samples grown with the same sequence of layers, except that one has only a thin InAs two-dimensional wetting layer (i.e., it contains no QDs) and the other has no InAs layer at all.

The conduction band profile of the device is shown in Fig. 1B. *X* and *Y* define the two main crystallographic axes, $[01\bar{1}]$ and $[\bar{2}33]$, respectively, of the (311) plane as shown in the inset. The layer of InAs QDs introduces a set of discrete electronic states below the GaAs conduction band edge. At zero bias, equilibrium is established by some electrons diffusing from the doped GaAs layers and filling the dot states. The resulting negative charge in the QW produces depletion layers in the region beyond the (AlGa)As barriers. When a voltage, *V*, is applied, resonant tunneling though a particular QD state leads to a peak in the current-voltage plot, *I*(*V*), whenever the energy of the state is resonant with an adjacent filled state in the negatively biased electron emitter layer, located at the left of the tunnel barriers.

In the low-temperature (T = 4.2 K) $I(V)$ characteristics in reverse bias (negative bias to emitter) in the presence of a magnetic field, *B*, applied parallel to the growth plane (*X*, *Y*) (Fig. 2), a series of resonant features labeled e_1 to e_7 are observed. The features are more clearly revealed in the differential conductance $G = dI/dV$ plot shown in the inset in Fig. 2A for B = 3.5 T. The amplitude of each resonance exhibits a strong dependence on the intensity of *B*. In particular, with increasing *B*, the low-voltage resonances (e_1 to e_3) decrease steadily in amplitude, whereas the others (e_4 to e_7) have a nonmonotonic magnetic field dependence. For example, e_5 is not visible at B = 0 T and develops with increasing field. The amplitude of all peaks is quenched at high field.

The resonant peaks are not observed in the two control samples and so are related directly to the presence of InAs QDs. For each resonant feature, we observe a thermally activated current onset, which is an unambiguous signature of an electron tunneling from a thermalized Fermi distribution of emitter states into an individual, discrete, and sharp QD energy level (*12*, *13*). Each resonance extends over a fairly wide voltage range (~10 mV). This is not surprising as it reflects tunneling from a broad energy distribution of occupied states in the emitter. The zero-dimensional states themselves have a much narrower linewidth. Previous tunnel current measurements at low temperatures on structures containing a large ensemble of QDs have also revealed the presence of resonant tunneling peaks due to individual dots in the range of bias close to the threshold of current flow (*13*–*18*). Here, we focus on the magnetic field dependence of the QD resonances and on how this provides detailed information about the form of the wave function associated with an electron in a QD.

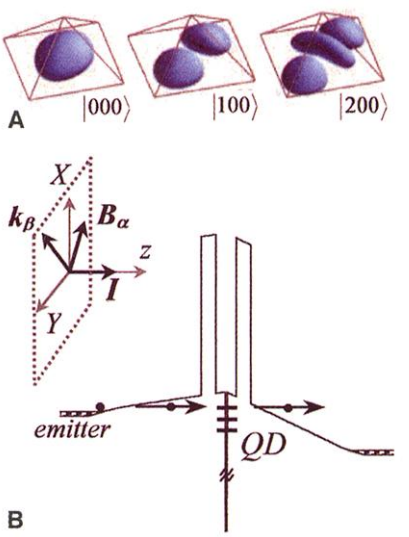

Fig. 1. (**A**) Probability density isosurfaces for the ground (|000⟩) and excited (|100⟩ and |200⟩) states of a pyramidal InAs/GaAs dot as calculated in (*10*). (**B**) Schematic conduction band profile under an applied bias of an *n-i-n* GaAs/(AlGa)As double-barrier resonant tunneling diode incorporating InAs self-assembled quantum dots (QDs). (**Inset**) Orientation of the magnetic field, *B*, and current, *I*, in the magnetotunneling experiment. *X* and *Y* define the two main crystallographic axis, $[01\bar{1}]$ and $[\bar{2}33]$, respectively, in the (311)-oriented GaAs substrate. α and β indicate, respectively, the direction of *B* and of the momentum *k* acquired by the tunneling electron because of the action of the Lorentz force.

[1]School of Physics and Astronomy, University of Nottingham, Nottingham NG7 2RD, UK. [2]Institute of Microelectronics Technology, Russian Academy of Sciences (RAS), 142432 Chernogolovka, Russia. [3]Department of Electronic and Electrical Engineering, University of Sheffield, Sheffield S1 3JD, UK.

*Permanent address: Institute of Microelectronics Technology, RAS, 142432 Chernogolovka, Russia.
†To whom correspondence should be addressed. E-mail: Laurence.Eaves@nottingham.ac.uk

The magnetic field dependence of the amplitude of the peak of the differential conductance is plotted (Fig. 2B) for each of the resonances, e_1 to e_7. We show $G(B)$ plots rather than $I(B)$ plots because the former allows us to identify more clearly the magnetic field dependence of each resonant feature. However, almost identical plots are obtained by plotting the B dependence of the measured values of the current or of the integrated current, $\int_{peak} I(V)dV$. The plots show three characteristic types of magnetic field dependence: Type I (peaks e_1, e_2, and e_3) shows a maximum in $G(B)$ at $B = 0$ T followed by an almost monotonic decay to zero at around 8 T; type II (e_4 and e_5) shows almost no conductance at $B = 0$ T, with $G(B)$ increasing to a broad maximum at ~4 T, followed by a gradual decay to zero; and type III (e_6 and e_7) shows two clear maxima in G at $B = 0$ T and ~5 T, with $G(B)$ falling to a minimum value of almost zero between these maxima. The behavior of the type II peaks is particularly interesting as it suggests that the associated tunneling transition is forbidden for $B = 0$ T but becomes allowed when the magnetic field is applied.

We can understand the magnetic field dependence of the resonances in terms of the effect of B on a tunneling electron. Let α, β, and z indicate the direction of B, the direction normal to B in the growth plane (X, Y), and the normal to the tunnel barrier, respectively (see Fig. 1B). When an electron tunnels from the emitter into the dot, it acquires an additional in-plane momentum given by (*19*)

$$k_\beta = eB\Delta s/\hbar \quad (1)$$

where Δs is the effective distance tunneled along z and $\hbar$ is Planck's constant divided by 2π. This effect can be understood semiclassically in terms of the increased momentum along β, which is acquired by the tunneling electron because of the action of the Lorentz force. In terms of mapping out the spatial form of an electronic state, we can envisage the effect of this shift in k space as analogous to that of the displacement, in real space, of the atomic tip in an STM imaging measurement.

The applied voltage allows us to tune resonantly to the energy of a particular QD state. Then, by measuring the variation of the tunnel current with B, we can determine the size of the matrix element that governs the quantum transition of an electron as it tunnels from a state in the emitter layer into a QD. In our experiment, the tunneling matrix element is most conveniently expressed in terms of the Fourier transforms $\Phi_{i(f)}(k)$ of the conventional real space wave functions (*20*, *21*). Here the subscripts i and f indicate the initial (emitter) and final (QD) states of the tunnel transition. Relative to the strong spatial confinement in the QD, the initial state in the emitter has only weak spatial confinement. Hence, in k space, $\Phi_i(k)$ corresponds to a sharply peaked function with a finite value only close to $k = 0$. As the tunnel current is given by the square of the matrix element involving $\Phi_i(k)$ and $\Phi_{QD}(k)$, the narrow spread of k for $\Phi_i(k)$ allows us to determine the form of $\Phi_{QD}(k)$ by varying B and hence k according to Eq. 1. Thus, by plotting $G(B)$ for a particular direction of B, we can measure the dependence of $|\Phi_{QD}(k)|^2$ along the k direction perpendicular to B. Then, by rotating B in the plane (X, Y) and making a series of measurements of $I(B)$

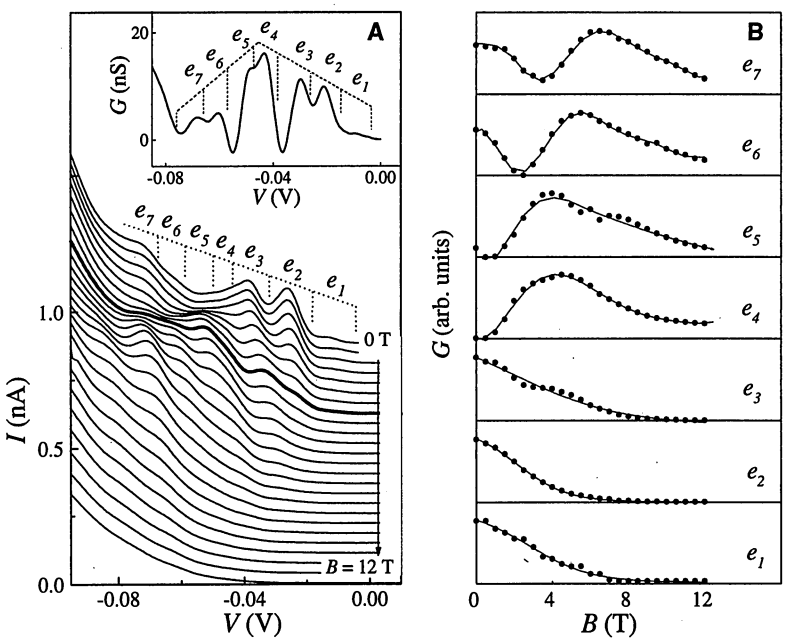

Fig. 2. (**A**) Low-temperature (T = 4.2 K) $I(V)$ characteristics in reverse bias (positive biased substrate) in the presence of a magnetic field, B, perpendicular to the current. B is increased in steps of 0.5 T, and the corresponding curves are displaced along the current axis for clarity. (Inset) Differential conductance, $G = dI/dV$, at $B = 3.5$ T. The corresponding $I(V)$ characteristic is plotted in the main part of the figure as a dark line. (**B**) Magnetic field dependence of the peak of G associated to the resonances e_1 to e_7 shown in (A). Continuous lines are guides for the eye.

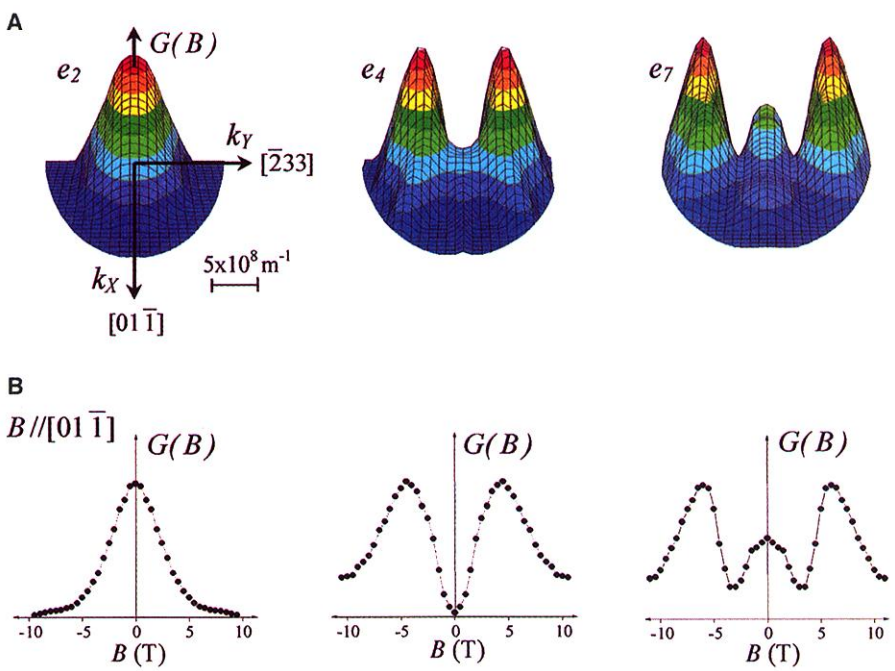

Fig. 3. (**A**) Distribution in the plane (k_X, k_Y) of the differential conductance, $G = dI/dV$, for three representative states. This provides a spatial map of $|\Phi_{QD}(k_X, k_Y)|^2$, the square of the Fourier transform, $\Phi_{QD}(k_X, k_Y)$, of the probability density of the electron confined in the dot. X and Y define the two main crystallographic axis, [01$\bar{1}$] and [$\bar{2}$33], respectively, in the ($\bar{3}$11)-oriented GaAs plane. (**B**) Dependence of G on magnetic field for B parallel and antiparallel to [01$\bar{1}$] for the same states shown in (A).

with B set at regular intervals ($\Delta\theta \sim 10°$) of the rotation angle θ, we obtain a full spatial profile of $|\Phi_{QD}(k_X, k_Y)|^2$. This represents the projection in k space of the probability density of a given electronic state confined in the QD.

The model provides a simple explanation of the magnetic field dependence of the resonant current features e_1 to e_7. In particular, the forbidden nature of the tunneling transition associated with e_4 and e_5 at $B = 0$ T is due to the odd parity of the final state wave function, which corresponds to the first excited state of a QD.

Figure 3A shows the spatial form of $G(B) \sim |\Phi_{QD}(k_X, k_Y)|^2$, in the plane (k_X, k_Y) for the three representative QD states corresponding to the peaks e_2, e_4, and e_7. The measured values of $G(B)$ for two directions of B, parallel and antiparallel to the [01$\bar{1}$] axis, are shown (Fig. 3B). The contour plots reveal the characteristic form of the probability density distribution of a ground state orbital and the characteristic lobes of the higher energy states of the QD. The electron wave function has a biaxial symmetry in the growth plane, with axes corresponding quite closely (within measurement error of 10°) to the main crystallographic directions [01$\bar{1}$] and [$\bar{2}$33]. In particular, detailed examination of the data reveals that the projected probability density of the ground state has an elliptical form, with the major axis along the [01$\bar{1}$] direction.

Although our measurements reveal detailed information about the symmetry of the QD wave functions with respect to the in-plane coordinates, they give us no information about the z dependence. This is directly related to the morphology of the QDs. In general, the dot height is much smaller than the dimensions of the base (*1*). Therefore, the quantization energy of confinement along z is much higher than that for in-plane motion. Our discussion of the magnetotunneling data has made two important and reasonable assumptions. The first is that the motion along z is separable from the in-plane motion. This approximation allows us to label the QD state using the quantum numbers n_1 and n_2 for the in-plane motion and n_3 for motion along z. Our second assumption is that all of the observed peaks involve final (QD) states that share the same type of quantum confinement along z, i.e., have the same value of n_3 (= 0).

In recent years, several different approaches have been used to calculate the eigenstates of QDs. They include perturbation effective mass approaches (*1*), eight-band $k \cdot p$ theory (*10*, *22*, *23*), and empirical pseudopotential models (*24*). Calculations generally depict the form of the wave functions as plots of the probability density in real space, $|\Psi_{QD}(r)|^2$. A tunnel current measurement can provide no information about the phase of the wave function, but, in general, the phase of $\Psi_{QD}(r)$ is easily obtained from a model calculation. Once the phase factor is known, it is a straightforward task for theoreticians to Fourier transform the calculations of the wave function into k space. A direct comparison could then be made with our spatial maps.

Our technique has allowed us to observe successive features in $I(V)$ corresponding to resonant tunneling through a limited number of discrete states whose wave functions display the symmetry of the ground state and first and second excited states of QDs. However, the simple device configuration does not permit us to determine whether an excited state peak and a ground state peak correspond to the same QD. This question could be resolved by experiments on structures with electrostatic gates (*18*).

Despite the large number of QDs in our sample (10^6 to 10^7 for a 100-μm-diameter mesa), we observed only a small number of resonant peaks over the bias range (~100 mV) close to the threshold for current flow. This behavior has been reported in earlier studies (*13*–*18*) and, although not fully understood, is probably related to the limited number of conducting channels in the emitter that can transmit electrons from the doping layer to the QDs at low bias. There is no reason to believe that the dots studied are atypical of the distribution as a whole.

Magnetotunneling spectroscopy provides us with a means of probing the spatial form of the wave functions of electrons confined in zero-dimensional QDs. The technique is both noninvasive and nondestructive and allows us to probe spatially quantum states that are buried hundreds of nanometers below the surface.

References and Notes

1. D. Bimberg, M. Grundmann, N. N. Ledentsov, *Quantum Dot Heterostructures* (Wiley, New York, 1999), and references therein.
2. J. Y. Marzin, J. M. Gerard, A. Izraël, D. Barrier, G. Bastard, *Phys. Rev. Lett.* **73**, 716 (1994).
3. R. J. Nötzel, J. Temmyo, T. Tamamura, *Nature* **369**, 131 (1994).
4. L. Landin, M. S. Miller, M.-E. Pistol, C. E. Pryor, L. Samuelson, *Science* **280**, 262 (1998).
5. A. P. Alivisatos, *Science* **271**, 933 (1996).
6. S. A. Empedocles and M. G. Bawendi, *Science* **278**, 2114 (1997).
7. M. F. Crommie, C. P. Lutz, D. M. Eigler, *Science* **262**, 218 (1993).
8. S. H. Pan *et al.*, *Nature* **403**, 746 (2000).
9. N. B. Zhitenev *et al.*, *Nature* **404**, 473 (2000).
10. O. Stier, M. Grundmann, D. Bimberg, *Phys. Rev. B* **59**, 5688 (1999).
11. A. Patanè *et al.*, *Phys. Rev. B*, in press.
12. A. K. Geim *et al.*, *Phys. Rev. Lett.* **72**, 2061 (1994).
13. P. C. Main *et al.*, *Phys. Rev. Lett.* **84**, 729 (2000).
14. M. Narihiro, G. Yusa, Y. Nakamura, T. Noda, H. Sakaki, *Appl. Phys. Lett.* **70**, 105 (1997).
15. I. E. Itskevich *et al.*, *Phys. Rev. B* **54**, 16401 (1996).
16. I. Hapke-Wurst *et al.*, *Semicond. Sci. Technol.* **14**, L41 (1999).
17. T. Suzuki, K. Nomoto, K. Taira, I. Hase, *Jpn. J. Appl. Phys. Part 1* **36**, 1917 (1997).
18. D. G. Austing *et al.*, *Appl. Phys. Lett.* **75**, 671 (1999).
19. R. K. Hayden *et al.*, *Phys. Rev. Lett.* **66**, 1749 (1991).
20. P. H. Beton *et al.*, *Phys. Rev. Lett.* **75**, 1996 (1995).
21. J. W. Sakai *et al.*, *Phys. Rev. B* **48**, 5664 (1993).
22. C. Pryor, *Phys. Rev. B* **57**, 7190 (1998).
23. W. Yang, H. Lee, T. J. Jonhson, P. C. Sercel, A. G. Norman, *Phys. Rev. B* **61**, 2784 (2000).
24. L.-W. Wang, J. Kim, A. Zunger, *Phys. Rev. B* **59**, 5678 (1999).

25. The work is supported by the Engineering and Physical Sciences Research Council (UK). A.L. gratefully acknowledges the support of the Fundação de Ampàro Pesquia do Estado de São Paulo Foundation (Brazil). E.E.V. and Y.V.D. gratefully acknowledge support from the Royal Society.

21 June 2000; accepted 16 August 2000

Potent Analgesic Effects of GDNF in Neuropathic Pain States

Timothy J. Boucher,[1] Kenji Okuse,[2] David L. H. Bennett,[1]* John B. Munson,[1] John N. Wood,[2] Stephen B. McMahon[1]†

Neuropathic pain arises as a debilitating consequence of nerve injury. The etiology of such pain is poorly understood, and existing treatment is largely ineffective. We demonstrate here that glial cell line–derived neurotrophic factor (GDNF) both prevented and reversed sensory abnormalities that developed in neuropathic pain models, without affecting pain-related behavior in normal animals. GDNF reduces ectopic discharges within sensory neurons after nerve injury. This may arise as a consequence of the reversal by GDNF of the injury-induced plasticity of several sodium channel subunits. Together these findings provide a rational basis for the use of GDNF as a therapeutic treatment for neuropathic pain states.

The neurotrophic factor GDNF promotes survival of a subgroup of developing sensory neurons (*1*). In adult animals, approximately 60% of dorsal root ganglion neurons normally express receptor components for GDNF (*2*, *3*), and this factor promotes neurite outgrowth in vitro and regeneration in vivo of both large- and small-caliber sensory neurons (*4*, *5*). GDNF is known to have neuroprotective effects on damaged adult sensory neurons, including the reversal of axotomy-induced changes in gene expression (*2*, *6*, *7*).